PHYSICAL REVIEW B **95**, 195156 (2017)

Crystal-electric-field excitations and spin dynamics in $Ce_3Co_4Sn_{13}$ semimetallic chiral-lattice phase

Kazuaki Iwasa[*]
Frontier Research Center for Applied Atomic Sciences & Institute of Quantum Beam Science, Ibaraki University, Tokai, Naka, Ibaraki 319-1106, Japan

Yuka Otomo, Kazuya Suyama, and Keisuke Tomiyasu
Department of Physics, Tohoku University, Sendai 980-8578, Japan

Seiko Ohira-Kawamura and Kenji Nakajima
Materials and Life Science Division, J-PARC Center, Japan Atomic Energy Agency, Ibaraki 319-1195, Japan

Jean-Michel Mignot
Laboratoire Léon Brillouin, CEA-CNRS, CEA/Saclay, 91191 Gif sur Yvette, France

(Received 8 April 2017; revised manuscript received 11 May 2017; published 26 May 2017)

Inelastic neutron scattering experiments have been conducted to investigate the spin dynamics and crystal-electric-field level scheme of the Ce $4f$ electrons in $Ce_3Co_4Sn_{13}$. This compound exhibits a large specific heat at low temperatures and anomalous semimetallic transport in the chiral crystallographic phase below 160 K. Distinctly observed magnetic excitations at approximately 6 and 29 meV are asymmetric in spectral shape and are reproduced by two inequivalent crystal-electric-field splitting schemes, which are deduced from the chiral structure. We have also observed the spin dynamics reflecting antiferromagnetic correlations below 1 meV, which is enhanced with an upturn in the electrical resistivity below 15 K and which yields a low-energy density of state relevant to the large specific heat. We discuss the possibility of a three-dimensional Weyl semimetal state, considering the chiral-lattice symmetry, electronic hybridization, and magnetic correlation.

DOI: 10.1103/PhysRevB.95.195156

I. INTRODUCTION

The Kondo effect is a typical quantum many-body effect influencing the electronic properties of metallic compounds [1]. The quasiparticle state associated with the screening of localized spins by conduction electrons favors a nonmagnetic ground state with a drastic enhancement of the carrier mass. Further, the electric conductivity exhibits a logarithmic dependence on the temperature in the metallic state, while the semiconductor state appears in the case of band-structure half filling. On the other hand, the symmetry effects on nontrivial electronic states are recently discovered and fascinating subjects. Topological insulators are characterized by the surface band state expressed by the Dirac cones [2], and Rashba-type spin-orbit coupling induces an electronic band splitting in a noncentrosymmetric system [3,4]. In addition, magnetic skyrmions are associated with the Dzyaloshinskii-Moriya interaction in a chiral structure [5]. Thus, the investigation of new electronic states originating from combinations of quantum many-body effects and the characteristic symmetries of material structures is a topic of broad and current interest.

The $Ce_3Co_4Sn_{13}$ compound has been hypothesized to be a heavy fermion (HF) system [6–9]. The specific heat divided by the temperature reaches approximately 4 $J/(K^2$ mol-Ce) at 0.7 K, and its value at zero temperature is estimated to be 75 mJ/(K^2 mol-Ce). The peak in the specific heat as a function of temperature is considered to reflect the emergence of magnetic short-range correlations [8]. No magnetic ordering has been observed down to 0.4 K [10]. However, the magnetic susceptibility above 100 K was analyzed based on the Curie–Weiss law, and the effective magnetic moment was evaluated as 2.56 μ_B/Ce, close to the value of 2.54 μ_B/Ce for the $4f^1$ configuration of the Ce^{3+} free ion [7]. Further, the electrical resistivity of $Ce_3Co_4Sn_{13}$ is much different from that of metallic $La_3Co_4Sn_{13}$ in the low-temperature range, and its temperature dependence is considerably weaker [7]. The electrical resistivity exhibits a slight kinklike upturn at a transition temperature $T_D = 160$ K, for which Lue *et al.* [11] have proposed a charge-density-wave (CDW) formation associated with the *p-d* hybridization between Sn and Co. Further, nuclear magnetic resonance (NMR) investigations of $RE_3Co_4Sn_{13}$ ($RE =$ La and Ce) have suggested that structural transitions with partial band-gap formation may occur at 152 and 155 K [11,12]. However, the upturn in the resistivity at T_D with decreasing temperature is enhanced under pressure [8,13]. This phenomenon is contrary to typical metallic-system phenomena in which pressure favors more dispersive bands and Fermi-surface recovery. The electrical resistivity exhibits an increase with decreasing temperature below 15 K, followed by a maximum at approximately 1 K, thereby indicating another characteristic energy scale for the electronic states in $Ce_3Co_4Sn_{13}$ [7,13]. Moreover, a neutron diffraction study has evidenced an antiferromagnetic peak induced by finite magnetic fields below 4.2 K [14]. At present, controversy exists regarding the coexistence of these phenomena, the HF state, the magnetic correlation, and the CDW state in $Ce_3Co_4Sn_{13}$. No electronic-state model to explain these various behaviors has yet been proposed.

Very recently, we succeeded in determining the crystal structure of $Ce_3Co_4Sn_{13}$ using synchrotron x-ray diffraction

---

[*] kazuaki.iwasa.ifrc@vc.ibaraki.ac.jp

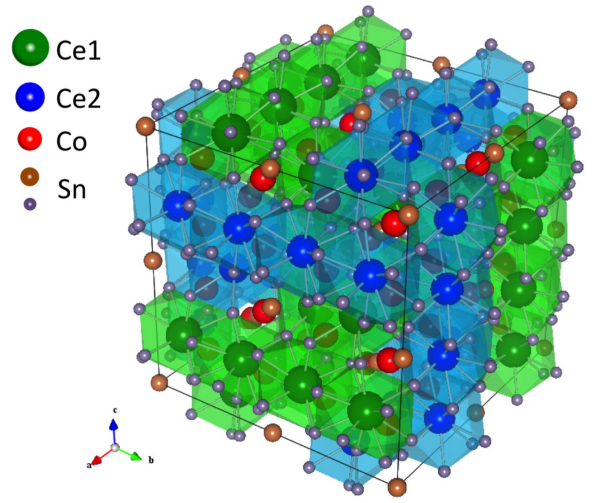

FIG. 1. Schematic of enantiomer of $Ce_3Co_4Sn_{13}$ chiral cubic structure in low-temperature I′ phase [15]. The Sn atoms form the cagelike unit shown by the shaded polyhedra and surround the two inequivalent Ce ions, Ce1 and Ce2, as shown by the green and blue columns, respectively.

measurements [15]. The crystal structure above $T_D \simeq 160$ K, belonging to the $Pm\bar{3}n$ space group (I phase, lattice constant $a = 9.601$ Å at 200 K) transforms to a structure with the $I2_13$ space group (I′ phase, lattice constant $a = 19.162$ Å), characterized by the wave vector $\boldsymbol{q} = (1/2,1/2,0)$ and its equivalents. The I′-phase structure is a chiral noncentrosymmetric lattice. One of the enantiomers is shown in Fig. 1.

In that study, we concluded that $La_3Co_4Sn_{13}$ undergoes the same crystal-structure transformation as $Ce_3Co_4Sn_{13}$, because $La_3Co_4Sn_{13}$ exhibits the same superlattice x-ray diffraction peaks below the same temperature $T_D \simeq 160$ K. In this structure, there are two inequivalent Ce-ion sites surrounded by neighboring Sn atoms, Ce1 and Ce2, which are indicated by the green and blue rows shown in Fig. 1. The Ce-Sn distances in the green Ce1 row range from 3.300 to 3.481 Å (3.397 Å in average). Those in the blue Ce2 rows range from 3.316 to 3.398 Å, and the average value is 3.359 Å. The Ce1-Sn cage is slightly larger than the Ce2-Sn cage. The multiplicities of the Ce1 and Ce2 are equivalent (the Wyckoff site 24*c*). Such inequivalent atomic sites often provide different electronic states, as will be discussed below in the context of experimental results. Note that the structural transformation is not fully explained by the model based on the previously proposed CDW formation [11]. That is, the Fermi surface does not vanish below T_D, because of the increases in the magnetic susceptibilities of $La_3Co_4Sn_{13}$ with decreasing temperature across T_D. The electron charge distributions of $Ce_3Tr_4Sn_{13}$ (Tr = Co, Ru, and Rh) have been studied on the basis of the band-structure calculation for the $Pm\bar{3}n$ crystal structure [16]. This previous investigation revealed a characteristic charge accumulation between Tr and Sn, which plays a role in the covalent bonding. Rearrangement of this accumulated charge may cause the structural transformation. In addition, it is suggested that the $I2_13$ space group produces the bulk chiral fermion and the Weyl semimetallic state [17]. We hypothesize that the Ce $4f$ electrons interacting with the conduction electrons contribute to the Fermi level tuning at the band crossing points, then facilitating the emergence of the low-carrier state. Therefore, as mentioned above, strongly correlated electrons on the chiral symmetry lattice can be examined in $Ce_3Co_4Sn_{13}$.

The present study aims to reveal the magnetic excitations relevant to the electric transport and magnetic properties of $Ce_3Co_4Sn_{13}$, which have remained undetermined following the evidence of the low-temperature chiral structure obtained in our previous study. We conclude that the spectrum in the 10-meV range can be explained by two inequivalent crystal-electric-field (CEF) level schemes. In addition, the low-energy spin dynamics below 1 meV evolves below approximately 15 K, the temperature at which the resistivity upturn appears. This spin dynamics is characterized by the emergence of spatial correlation with dominant antiferromagnetic fluctuation; therefore, the transport anomaly, as well as the large specific heat value, is closely correlated with the dispersing spin dynamics. We also discuss the possibility of the existence of the Weyl semimetal for the high-resistivity state in the chiral-structure phase of $Ce_3Co_4Sn_{13}$.

II. EXPERIMENTAL DETAILS

Samples of $RE_3Co_4Sn_{13}$ (RE = La and Ce) were synthesized via the molten Sn-flux method [7,18–20]. We succeeded in obtaining single crystals with maximum dimensions of 7 mm from Ce (3N), Co (4N), and Sn (5N) starting materials.

Inelastic neutron scattering (INS) experiments for powdered samples were performed by using the AMATERAS cold-neutron disk chopper spectrometer installed at the pulsed-neutron beam line BL14 at the Materials and Life Science Experimental Facility, J-PARC [21]. We measured the INS spectra of $Ce_3Co_4Sn_{13}$ and $La_3Co_4Sn_{13}$ specimens with the same mass and extracted the $4f$-electron contribution from the difference between the data for these two compounds. Several incident neutron energies were selected via chopper combination. The energy resolutions corresponding to the full width at half maximum (FWHM) at the elastic scattering position were approximately 2.3, 0.46, and 0.051 meV for the incident neutron energies of $E_i = 42.0$, 15.14, and 3.13 meV, respectively. The UTSUSEMI software suite was used to analyze the spectral data obtained via the pulsed-neutron scattering technique [22].

INS experiments were also performed on four co-aligned single-crystalline samples of $Ce_3Co_4Sn_{13}$ on the 4F2 cold-neutron triple-axis spectrometer at the Orphée reactor of Laboratoire Léon Brillouin. The detected final neutron energy was $E_f = 3.5$ meV, and the energy resolution at the elastic scattering condition was 0.19 meV. Measurements were conducted using incident-neutron constant monitor counts. The sample temperatures were controlled using a closed-cycle refrigerator and a liquid-helium cryostat for AMATERAS and 4F2, respectively.

III. RESULTS AND ANALYSIS

A. INS results for polycrystalline sample

In this section, we will show the INS results for the polycrystalline sample, which was subsequently used for

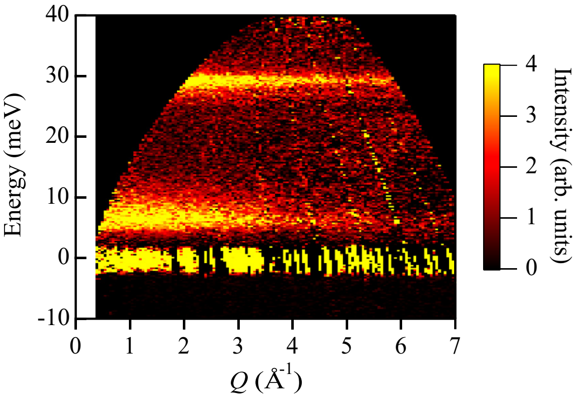

FIG. 2. Magnetic INS intensity contour map for $Ce_3Co_4Sn_{13}$ polycrystalline sample at 6 K. The incident neutron energy is $E_i = 42.0$ meV. The data correspond to the spectral difference between the Ce- and La-based compounds.

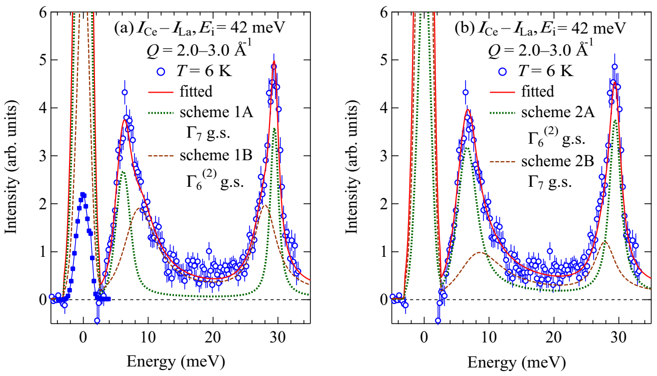

FIG. 3. Blue open circles are magnetic INS spectra for the $Ce_3Co_4Sn_{13}$ polycrystalline sample at 6 K by using the $E_i = 42.0$ meV setup. These data points shown in (a) and (b) are identical, and they correspond to the spectral differences between the Ce- and La-based compounds. The intensity was evaluated by integration over the scattering-vector-magnitude range of $Q = 2.0$–3.0 Å^{-1}. Solid squares in (a) are incoherent-scattering intensity of $Ce_3Co_4Sn_{13}$ multiplied by 1/200, FWHM of which is 2.31 meV corresponding to the energy resolution. (a) and (b) show the results of model 1 and 2 for the CEF analysis, respectively, as described in detail in the main text. The green dotted and brown broken lines are the fitted spectral components, and the red lines are total.

an analysis of the Ce $4f$-electron CEF schemes. Figure 2 shows a contour map of the INS intensity measured with $E_i = 42.0$ meV for the $Ce_3Co_4Sn_{13}$ polycrystalline sample.

The result was obtained by subtracting the data for an identically sized sample of the reference material, $La_3Co_4Sn_{13}$. The strong intensities at 6.4 and 29.4 meV are clearly apparent. These peaks are consistent with the previously reported energy spectrum obtained based on the INS [10]. The peak energies are independent of the magnitude of the scattering wave vector Q, while the intensity decreases monotonically with increased Q. The intensity dependence on Q follows the squared magnitude of the magnetic form factor of the Ce^{3+} $4f^1$ electronic state. This result indicates that the observed INS spectra correspond to the magnetic scattering due to the transitions between the CEF levels of the Ce $4f$ electrons.

The blue circles in Fig. 3(a) show the spectrum measured at 6 K, which were evaluated via intensity integration over the results obtained for the range of $Q = 2.0$–3.0 Å^{-1} in Fig. 2. It is noteworthy that each peak has an asymmetric spectral shape, despite the fact that we chose the spectrometer chopper combination to achieve a symmetrical resolution function. This result indicates that the Ce-ion site is nonuniform. Similar INS peaks are also apparent for the spectral data measured at 170 K above the structural-transition temperature T_D, as indicated by the black squares in Fig. 4. The intensity in the positive energy region, corresponding to the neutron-energy loss side, is suppressed compared to that at 6 K, and the peaks appear on the negative-energy side. These experimental facts also support the magnetic INS between the CEF splitting levels. Detailed analysis of this aspect is presented below (Sec. III B).

Figure 5 shows the excitation spectra obtained at 6 K using a lower incident energy $E_i = 15.14$ meV. The observed INS peak centered at 6.4 meV has an asymmetric spectral shape, as described for the data obtained for $E_i = 42.0$ meV shown in Fig. 3(a). This result also strongly supports the nonuniform $4f$-electron state in the chiral-lattice phase.

Figure 6 shows the low-energy excitation spectra obtained using $E_i = 3.13$ meV. A clear inelastic spectrum appears below ~1 meV at 6 K (blue circles), in marked contrast to the broad spectrum obtained at 170 K (red squares) corresponding to paramagnetic scattering. The previous INS study also demonstrated this low-energy response [10], and the present data confirm this excitation more precisely. Considering the CEF splitting schemes discussed above, we expect a modification of the CEF ground state due to interactions between the Ce $4f$ electrons, the energy scale of which corresponds approximately to 1 meV. A detailed INS investigation for the single-crystalline sample will be presented in Sec. III C.

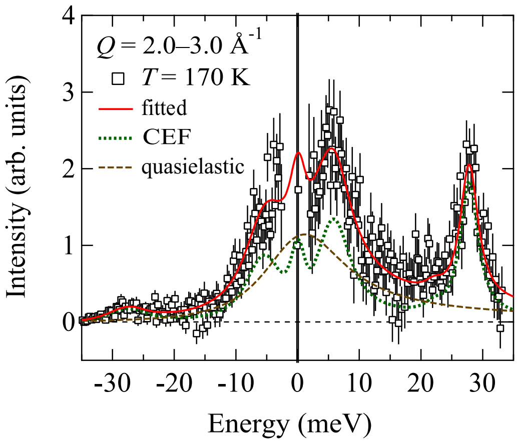

FIG. 4. Magnetic INS spectra for $Ce_3Co_4Sn_{13}$ polycrystalline sample at 170 K. The incident neutron energy is $E_i = 42.0$ meV. The intensity was evaluated by integration over the scattering-vector-magnitude range of $Q = 2.0$–3.0 Å^{-1}. All the data sets correspond to the spectral differences between the Ce- and La-based compounds. The red line is the results of the least-squares fitting analysis using the CEF model. The green dotted and brown broken lines are the fitted spectral components, as described in detail in the main text.

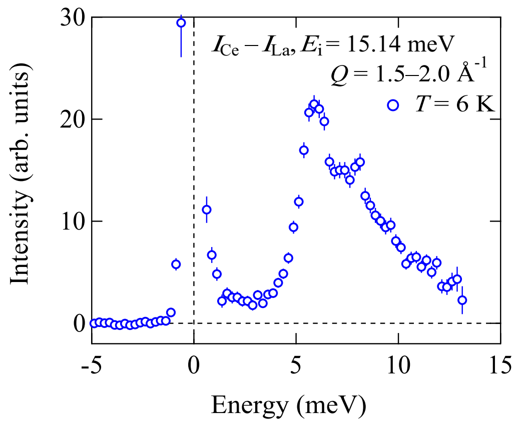

FIG. 5. Magnetic INS spectra for $Ce_3Co_4Sn_{13}$ polycrystalline sample at 6 K. The incident neutron energy is 15.14 meV. The intensity was evaluated by integration over the $Q = 1.5$–2.0 Å^{-1} range. The data set corresponds to the spectral difference between the Ce- and La-based compounds.

B. CEF analysis of polycrystalline-sample data

The spectra obtained using the $E_{\mathrm{i}} = 42.0$ meV setup were analyzed on the basis of the excitations between the CEF-split levels, which has not been determined precisely in the previous study [10]. As mentioned above, our previous x-ray structural analysis shows that $Ce_3Co_4Sn_{13}$ crystallizes in a cubic structure represented by the $Pm\bar{3}n$ space group above T_{D} and in that corresponding to $I2_13$ below T_{D}. The local symmetry at the Ce-ion site under $Pm\bar{3}n$ is D_{2d}; thus, the CEF Hamiltonian at the Ce site is expressed as

$$\mathcal{H}_{\mathrm{CEF}} = W\left[\frac{x_1}{2}O_2^0 + \frac{x_2}{60}O_4^0 + \frac{1-|x_1|-|x_2|}{12}O_4^4\right], \tag{1}$$

where the O_m^n are Stevens operators [23]. Using a set of basis wave functions for the total angular momentum $J = 5/2$ for the Ce^{3+} $4f^1$ configuration, we have diagonalized this Hamiltonian to obtain eigenfunctions of the three Kramers doublets, Γ_7, $\Gamma_6^{(1)}$, and $\Gamma_6^{(2)}$. The scattering function is expressed as $S(\boldsymbol{Q},E) = [n(E)+1]\chi''(\boldsymbol{Q},E)$, where $\chi''(\boldsymbol{Q},E)$ is the imaginary part of the generalized magnetic susceptibility and $n(E)$ is the Bose-Einstein distribution function. According to Marshall and Lowde [24], $\chi''(\boldsymbol{Q},E)$ for the CEF splitting state is represented by

$$\chi''(Q,E) \propto f^2(\boldsymbol{Q})E\frac{1}{Z}\left[\sum_{i,f}^{(E_i=E_f)} |\langle f|\boldsymbol{J}_\perp|i\rangle|^2 \frac{e^{-\frac{E_i}{k_{\mathrm{B}}T}}}{k_{\mathrm{B}}T}F_{if}(E) + \sum_{i,f}^{(E_i\neq E_f)} |\langle f|\boldsymbol{J}_\perp|i\rangle|^2 \frac{e^{-\frac{E_i}{k_{\mathrm{B}}T}} - e^{-\frac{E_f}{k_{\mathrm{B}}T}}}{E_f - E_i}F_{if}(E)\right], \tag{2}$$

where $f(\boldsymbol{Q})$ is the magnetic form factor. E_m and E_n are the respective energy eigenvalues of the initial and final states, $|m\rangle$ and $|n\rangle$, which are relevant to the scattering process due to the dipole operator $\boldsymbol{J}_\perp$. Z is the partition function. We assumed the Lorentzian spectral function $F_{mn}(E) = \gamma_{mn}/[(E-\Delta_{mn})^2 + \gamma_{mn}^2]$, with $\Delta_{mn} = E_n - E_m$.

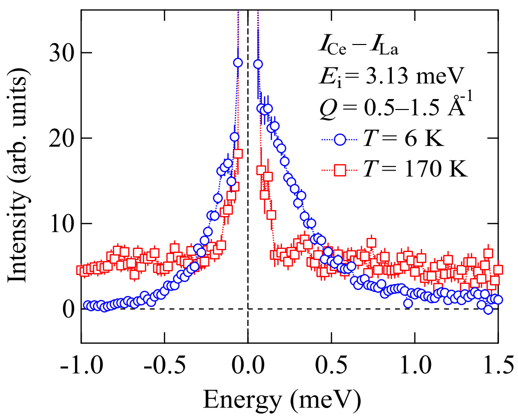

FIG. 6. Magnetic INS spectra for $Ce_3Co_4Sn_{13}$ polycrystalline sample at 6 and 170 K. The incident neutron energy is 3.13 meV. The intensity was evaluated by integration over the $Q = 0.5$–1.5 Å^{-1} range. The data set corresponds to the spectral difference between the Ce- and La-based compounds.

A least-squares fitting based on Eq. (2) and the Lorentzian $F_{mn}(E)$ to the obtained data was performed. In order to evaluate the excitation-peak width, we incorporated a procedure for convolution of the spectrometer resolution. We calculated an energy-transfer (E) dependence of the resolution FWHM, ΔE, for the $E_{\mathrm{i}} = 42.0$ meV setup by taking into account the spectrometer configuration: $\Delta E = 2.00, 1.50$, and 0.54 meV at $E = 0$, 8, and 30 meV, respectively [25]. As indicated in Sec. II and the incoherent-scattering intensity (Fig. 3), the FWHM at the elastic-scattering position is 2.31 meV. This value is slightly larger than the calculated value, because of a sample-size effect and an uncertainty of the incident-neutron time-of-flight spectrum. We assume that the aforementioned calculated ΔE multiplied by 2.31/2.0 is the resolution for the present measurement.

The fitting result for the 170 K data is shown by the solid line in Fig. 4. A quasielastic spectrum with an intrinsic spectral half width at half maximum (HWHM) of 7.5 meV is also incorporated, as indicated by the brown broken line, in addition to the CEF component shown by the green dotted line. The resultant $\mathcal{H}_{\mathrm{CEF}}$ parameters, the eigenstates, the eigenenergies, and the spectral widths are listed in the right column of Table I. The ground state is assigned to the $\Gamma_6^{(2)}$ wave function.

The same analysis was applied to the data obtained at 6 K. According to our previous structural determination, the low-temperature I′ phase is categorized in $I2_13$, which yields two inequivalent Ce-ion sites. These two sites are characterized by the averaged interatomic distance between the Ce and the neighboring Sn atoms: 3.397 and 3.359 Å for the Ce1 and Ce2 sites, respectively. Thus, we hypothesize that these two Ce-ion sites are under different CEF potentials and that two inequivalent level schemes appear in the I′ phase with the same probability, because both of the Ce1 and Ce2 ions are located at the Wyckoff site 24c. Such site-dependent CEF schemes for the Ce ions in the $Ce_3Pd_{20}Si_6$ HF compound have been evidenced by previous neutron scattering measurements [26]. This hypothesis implies four individual excitation peaks from the ground states of the two schemes and is consistent with the

TABLE I. The CEF parameters (W,x_1,x_2), the eigenstates together with the eigenenergies (E), and the spectral widths (γ) determined by the least-squares fitting analysis for the datasets at 6 and 170 K obtained by the $E_{\mathrm{i}} = 42$ meV condition.

	Model 1 for 6 K		Model 2 for 6 K		
CEF scheme	1A	1B	2A	2B	Model for 170 K
W (meV)	9.35(2)	7.79(13)	8.30(5)	8.18(14)	7.87(16)
x_1	0.191(2)	0.304(14)	0.317(3)	0.253(10)	0.317(18)
x_2	$-$ 0.250(3)	0.358(12)	0.300(9)	$-$ 0.215(22)	0.287(28)
ground state (g.s.)	Γ_7	$\Gamma_6^{(2)}$	$\Gamma_6^{(2)}$	Γ_7	$\Gamma_6^{(2)}$
1st ex. state and E (meV)	$\Gamma_6^{(2)}$ 6.04	Γ_7 8.14	Γ_7 6.38	$\Gamma_6^{(2)}$ 7.58	Γ_7 5.69
2nd ex. state and E (meV)	$\Gamma_6^{(1)}$ 29.4	$\Gamma_6^{(1)}$ 27.9	$\Gamma_6^{(1)}$ 29.4	$\Gamma_6^{(1)}$ 27.8	$\Gamma_6^{(1)}$ 27.8
γ (meV) [g.s. → 1st]	0.62(27)	2.68(27)	1.31(37)	3.83(74)	3.0(1.4)
γ (meV) [g.s. → 2nd]	0.60(15)	2.01(32)	0.97(19)	1.84(53)	1.66(61)

asymmetric spectral shape shown in Fig. 3(a). In fact, the point group at these Ce-ion sites in the I′ phase is C_1, the symmetry of which is lower than that in the high-temperature I phase (D_{2d}). However, we simply assume that the additional terms in the CEF Hamiltonian owing to C_1 contribute significantly less than those for D_{2d}, because of the slight atomic displacements from the I phase to the I′ phase. Therefore, in this study, we applied the same CEF Hamiltonian, $\mathcal{H}_{\mathrm{CEF}}$, given by Eq. (1) to analyze the data obtained for the I′ phase.

We have systematically searched CEF-level schemes within the space of the two sets of CEF parameters, W, x_1, and x_2, in order to reproduce the experimental result. We hypothesize a constraint of the same site multiplicity for Ce1 and Ce2 in the I′ phase. We found two alternative CEF models, each of which is comprised of the two level schemes for Ce1 and Ce2. Both of these models reproduce the experimental data at 6 K well with similar fitting quality. The result for model 1 is indicated by the red solid line in Fig. 3(a). The determined parameters and the eigenstates are listed in Table I.

The CEF parameter set, scheme 1A, which gives the result indicated by the green dotted line, is comprised of the Γ_7 ground state. It is noteworthy that the ground-state wave function is not identical to that in the high-temperature I phase. The parameter set, scheme 1B, is comprised of the $\Gamma_6^{(2)}$ ground state, which corresponds to the brown broken line in Fig. 3(a). The ground state in scheme 1B is conserved across the structural phase transition. As mentioned above, the total fitted result shown by the red solid line reproduces the experimental data very well. The spectral widths γ_{mn} for the first excited states are 0.62 and 2.68 meV for the CEF parameter sets of schemes 1A and 1B, respectively, and those for the second excited states are 0.60 and 2.01 meV, respectively. The broader spectral widths of scheme 1B can be attributed to the Ce2 site having shorter averaged interatomic distances to the surrounding Sn, because a stronger hybridization effect between the Ce $4f$ electrons and carriers (c-f hybridization) is expected for the shorter atomic distance. In addition, the spectral widths of scheme 1B are closer to those obtained for the 170-K data; thus, the $\Gamma_6^{(2)}$ ground state seems to be favorable for the strong hybridization. Here, we should remind the crystal structure of the I′ phase shown in Fig. 1, in order to check the CEF spectral broadening due to the nonuniform atomic arrangements around the Ce sites. The crystal structure is comprised of the Ce1 and Ce2 sites, which are characterized by polyhedra composed of the centered Ce atom and the neighboring Sn atoms. The polyhedra in the Ce1 row are equivalent with respect to the $I2_13$ space-group symmetry operations of the twofold rotation axes, which are perpendicular to and bisecting the row. Those in the Ce2 row are in the same manner. Therefore, the Ce1 and Ce2 sites carry their respective unique CEF schemes. This fact supports that the observed spectral widths based on the assumption of the two individual CEF schemes correspond to the hybridization strengths.

The second CEF-analysis result (model 2) is shown in Fig. 3(b). The data are the same as in Fig. 3(a). The parameters and the eigenstates are also listed in Table I. The green line (scheme 2A) and the brown line (scheme 2B) in Fig. 3(b) are based on the $\Gamma_6^{(2)}$ and Γ_7 ground states, respectively. The spectral widths for the first and second excited states in scheme 2A are 1.31 and 0.97 meV, respectively, while those in scheme 2B are much larger values 3.83 and 1.84 meV, respectively. The ground state exhibiting the broad spectrum in scheme 2B is Γ_7, in contrast to the $\Gamma_6^{(2)}$ ground state producing the broad spectra in scheme 1B.

We examined whether the Γ_7 ground state schemes 1A and 2B are consistent with the measured data at 170 K. The calculation gives a pronounced peak at approximately 22 meV corresponding to the excitation from the first excited state to the second excited one. This result indicates that the CEF scheme in the I-phase $Pm\bar{3}n$ structure is explained only by the aforementioned $\Gamma_6^{(2)}$ ground state. This finding indicates that the CEF model 1 for the data at 6 K is reasonable, because the broader spectrum for the $\Gamma_6^{(2)}$ ground state is common.

In addition to the aforementioned CEF-scheme models 1 and 2 summarized in Table I, we obtained another CEF-scheme candidate reproducing the experimental data at 6 K shown in Fig. 3. The parameter set is $W = 8.30(16), x_1 = 0.318(1), x_2 = 0.300(2)$ (scheme 3A) and $W = 5.80(24), x_1 = -0.274(20), x_2 = 0.801(30)$ (scheme 3B). Although the residual sum of squares for the fitting analysis of this parameter set is larger by 14% than those of the model 1 and 2, this is also consistent with the observed data. It is noteworthy that the CEF-level sequence of scheme 3A and 3B are not equivalent. This fact is consistent with the magnetic-field-induced antiferromagnetic reflection [14], as discussed for the models 1 and 2. The scheme 3A takes the same level sequence as those of schemes 1B and 2A, while scheme 3B is a different sequence ($\Gamma_6^{(1)}$-$\Gamma_6^{(2)}$-Γ_7) from those of 1A and 2B as well as 3A. More precise examination of the CEF schemes embedded in the I′ structure ($I2_13$) can be performed by a determination of magnetic-moment distribution using a polarized-neutron diffraction technique, which will be conducted in the near future.

It is noteworthy that the two different ground-state schemes are necessary for reproducing the experimental results at 6 K in the I′ ($I2_13$) structure comprised with the two individual Ce-ion sites. We have examined the model associated with the same ground states for the two schemes. However, such a model does not succeeded in reproducing the spectral intensity obtained at 6 K.

C. Low-energy INS results for single-crystalline sample

We also performed low-energy INS measurements on the single-crystalline sample using the 4F2 cold neutron triple-axis spectrometer. This measurement aims at revealing the low-temperature anomalies of the electrical-resistivity enhancement in the I′ phase [7,13] and the large specific heat below 1 K [6,8].

The measured data are shown in Fig. 7. Here, we denote the scattering vector $\boldsymbol{Q}$ in units of the reciprocal lattice in the I phase. Clear INS intensities are apparent in the 1.4-K data near the antiferromagnetic reciprocal point $\boldsymbol{Q} = (1,0,0)$, whereas the intensity at 20 K is suppressed. We measured the scattering vector dependence of the INS intensity along the [1 0 0] axis. The results show that the strong intensity below 0.4 meV in the $\boldsymbol{Q} = (1,0,0)$ data set shifts to the higher-energy region with $\boldsymbol{Q}$ varying up to (1.5,0,0). The $\boldsymbol{Q}$-dependent spectral shape means that the excitation is dispersive and cannot be ascribed to a single-ion CEF excitation.

We have least-square fitted the 1.4-K data to the magnetic response function form [27]

$$S(E) \propto \frac{E}{2\pi}\frac{1}{1-\mathrm{e}^{-E/k_\mathrm{B}T}} \times \sum_{n=1}^{2}\left[\frac{\gamma_n}{(E-\delta_n)^2+\gamma_n^2}+\frac{\gamma_n}{(E+\delta_n)^2+\gamma_n^2}\right], \qquad (3)$$

together with a Gaussian form for the elastic peak, which was deduced from a fit of the data at 20 K. Because a single Lorentzian function does not successfully reproduce the spectral shapes, two excitations indexed by $n = 1$ and 2 were also considered. This assumption may also be supported by the two inequivalent Ce-ion sites. The fitted results are represented by solid lines in Fig. 7, and the blue broken and black dotted lines are the components of $n = 1$ and 2, respectively. The energy positions δ_n are shown as functions of the magnitude of the reduced wave vector $\boldsymbol{q}$ along the [1 0 0] direction in Fig. 8(a).

The higher-energy component disappears at the larger $\boldsymbol{q}$ position; thus, the data points at $q = 0.5$ (r.l.u.) and $E = 0.6$ meV are ambiguous. However, the excitation energies having an unambiguous dependence on $\boldsymbol{Q}$ indicate a dispersion relation in the spin fluctuation. Figure 8(b) shows the temperature dependencies of the magnetic excitation intensities at $E = 0.25$ and 0.3 meV for $\boldsymbol{Q} = (1,0,0)$ and (1.5,0,0), respectively. Both increase with decreasing temperature below approximately 15 K, where the electrical resistivity exhibits an upturn [7,13].

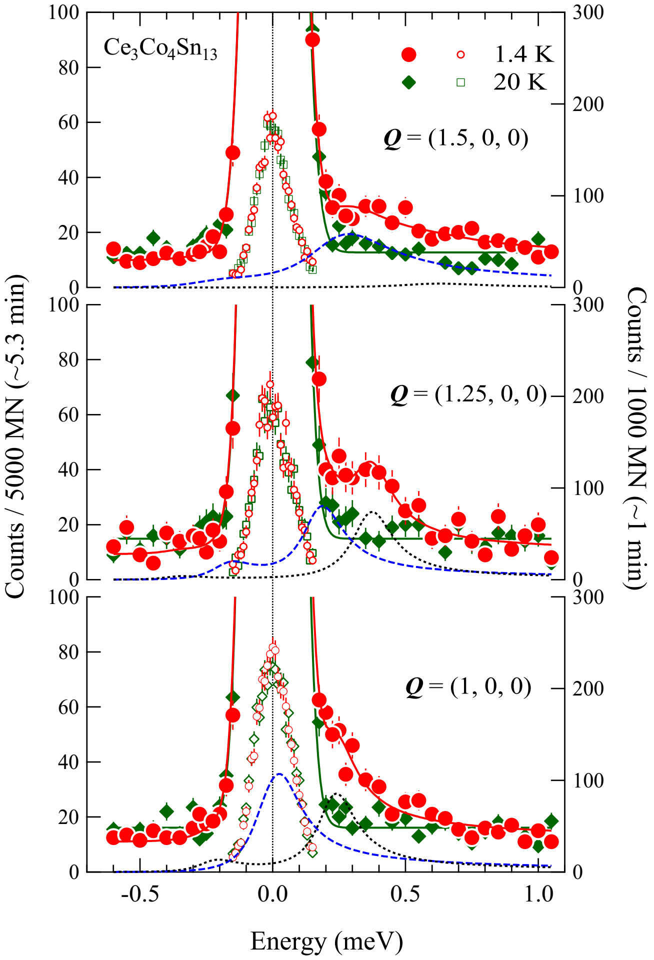

FIG. 7. INS spectra for $\boldsymbol{Q} = (1,0,0)$, (1.25, 0, 0), and (1.5, 0, 0) measured at 1.4 and 20 K, indicated by red circles and green diamonds, respectively. The left and right ordinates are for the inelastic response and the incoherent elastic part, respectively. The solid lines on the data points are the fitted results. The INS components for the 1.4-K data are shown by the blue broken lines and black broken lines.

IV. DISCUSSION

A. Magnetic properties

Here, we compare the present INS results for the Ce$_3$Co$_4$Sn$_{13}$ chiral-lattice phase with the electronic and magnetic properties previously reported in the literature. According to the present analysis of the CEF level schemes, the ground states $\Gamma_7(|\pm 1/2\rangle)$ (schemes 1A or 2B) and $\Gamma_6^{(2)}(\mp\alpha|\pm 5/2\rangle \pm \sqrt{1-\alpha^2}|\mp 3/2\rangle)$ (schemes 1B or 2A), are inequivalent. These two sites carry magnetic-moment eigenvalues of 0.43 and 1.1 μ_B/Ce, respectively. Previously published data on the field-dependent magnetization, $M(H)$, at 2 K has been explained as being due to a doubly degenerate ground state, which has an effective saturation magnetic

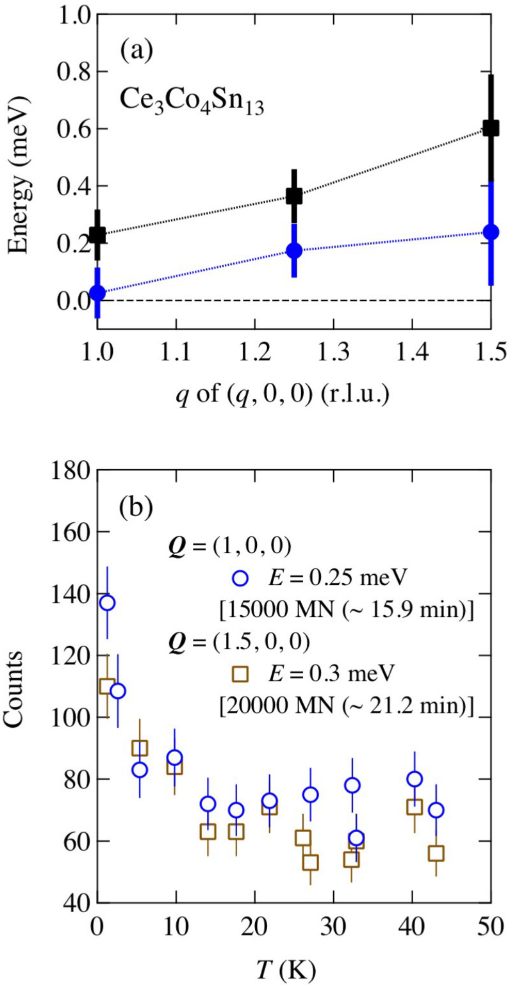

FIG. 8. (a) Magnetic excitation peak positions, δ_n ($n = 1$ and 2), as functions of the magnitude of the reduced wave vector $\boldsymbol{q}$ along the [1 0 0] direction. The vertical bars on the data points are spectral widths evaluated in the fitting analysis. (b) Temperature dependencies of magnetic excitation intensities at $E = 0.25$ and 0.3 meV for $\boldsymbol{Q} =$ (1,0,0) and (1.5,0,0), respectively.

moment of 0.64 μ_B/Ce [7]. This magnitude is relatively close to 0.77 μ_B/Ce, which is the average of the 0.43 and 1.1 μ_B/Ce values obtained from the CEF analysis in this study. The distinctly different magnitudes of the ground-state moments are also consistent with the previous observation of the neutron-diffraction peak induced under finite magnetic fields at $\boldsymbol{Q} = (1,0,0)$, which is the forbidden reflection point for the I-phase crystal structure [14]. This result suggests that the ferrimagnetic-moment distribution appears under magnetic fields in the low-temperature region, although no spontaneous long-range magnetic ordering occurs.

We also wish to mention the magnetic excitations of the $Ce_3Rh_4Sn_{13}$ isomorphic compound. This material also exhibits a semiconductor or semimetal behavior, similar to $Ce_3Co_4Sn_{13}$ [28,29]. We observed the structural phase transition at approximately 350 K characterized by the same superlattice vector as in the case of $Ce_3Co_4Sn_{13}$, which implies chiral-lattice formation in both of these compounds [30]. The INS spectrum of $Ce_3Rh_4Sn_{13}$ has been measured by Adroja *et al.* [31], and their data yield an asymmetric spectral shape, similar to that observed for $Ce_3Co_4Sn_{13}$ in the present study. From this accumulation of experimental data, we naturally expect that the magnetic excitations in both $Ce_3Co_4Sn_{13}$ and $Ce_3Rh_4Sn_{13}$ originate from a minimum of two inequivalent level schemes.

B. Low-energy spin excitation

We have observed a magnetic excitation mode below approximately 1 meV near $\boldsymbol{Q} = (1,0,0)$. As noted above, this excitation exhibits a clear momentum dependence, thereby indicating the emergence of intersite correlations. The data for the polycrystalline sample, shown in Fig. 6, correspond to the spin-excitation density of states, because the integration is conducted over a wide Q range. Within the observed excitations, the maximum of the excitation density of states is estimated to be at approximately 0.2 meV. This excited-energy value is consistent with the magnetic specific heat, which has a broad peak located at 0.7 K [6], by assuming a Schottky-type specific heat. This result indicates that the high value of the electronic specific heat estimated previously is not due to the conventional HF alone.

As shown in Fig. 8(b), the temperature dependencies of the magnetic excitation intensities exhibit an upturn with decreasing temperature below 15 K. The emergence of dispersing spin dynamics within the Kramers doublet ground states are closely correlated with the anomalous enhancement of the electrical resistivity below approximately 15 K [8,13]. This abrupt emergence of a dispersive spin excitation at low temperature is in contrast to the well-established HF systems, which exhibit magnetic quasielastic scattering. For example, the quasielastic scattering of $Ce_3Pd_{20}Si_6$, the intensity of which varies in the momentum space, shows the $\sqrt{T}$ law for the spectral width in a wide temperature range up to 100 K [27]. Thus, we state that the behavior for $Ce_3Co_4Sn_{13}$ is in marked contrast to the simple HF case.

A previous neutron diffraction study has investigated the magnetic-field-induced reflection at $\boldsymbol{Q} = (1,0,0)$ [14]. The magnetic-field dependencies of the intensities at 0.14 and 4.2 K were analyzed using the Brillouin function for an effective spin-1/2 state. Hence, the authors noted that this single-site model failed to reproduce the excess intensity appearing near 2 T at 0.14 K, and considered this result to signify a crossover from short-range order to single-impurity Kondo behavior with increasing magnetic fields. However, the present study evidences that the dispersing spin excitation emerges and the HF behavior are less significant than previously expected. These phenomena should be considered when interpreting this anomaly in the magnetization process.

Adroja *et al.* reported the low-energy spin dynamics for $Ce_3Rh_4Sn_{13}$ [31]. Recently, we initiated a measurement of this low-energy signal using our own $Ce_3Rh_4Sn_{13}$ sample, and successfully detected a tiny enhancement of the INS intensity below 15 K [32]. Thus, similar spin dynamics arises in these isomorphic Ce-based 3-4-13 materials exhibiting semiconductor or semimetal behavior. It is a subject for further investigation to determine whether the observed low-energy spin dynamics, as well as the semimetal states in $Ce_3Co_4Sn_{13}$

and $Ce_3Rh_4Sn_{13}$, is associated with the chiral fermions to which the Ce $4f$ electrons contribute.

C. Possible Weyl semimetal in chiral symmetry phase

In this section, we will discuss a possibility of the Weyl semimetal state in the chiral-lattice phase of $Ce_3Co_4Sn_{13}$, because the anomalous high resistivity is not simply explained by the HF state or the Kondo semiconductor.

Several arguments regarding a semimetal associated with the Dirac or Weyl fermion in a three-dimensional system have been presented [33]. The example materials are Na_3Bi [34], Cd_3As_2 [35], TaAs [36,37], and others. According to the theoretical classification [17], the chiral $I2_13$ space group is expected to give rise to a bulk chiral fermion and a three-dimensional Weyl semimetallic state. The studies on the bulk Weyl fermion, which are cited in the next paragraph, are helpful to understand the unsettled phenomena through which the resistivity retains a high value below T_D in particular, and increases further below 15 K in the chiral-lattice phases of $Ce_3Tr_4Sn_{13}$.

The electrical resistivity of $Ce_3Co_4Sn_{13}$ is significantly higher than that of $La_3Co_4Sn_{13}$ [7,13], although the same structural phase transition occurs at T_D [15]. In addition, because the CEF excitation spectrum is broad as shown in the present study, one can assume that the c–f hybridization plays a role in the transport properties. On the other hand, the electrical resistivity does not diverge down to the minimum measurement temperature of 0.2 K [13]. Therefore, no full gap similar to that occurring in an ideal Kondo semiconductor is formed. In order to understand the low-temperature electronic state of $Ce_3Co_4Sn_{13}$, we refer to a study on the impurity Kondo effect associated with three-dimensional Weyl fermions, in which a theoretical classification of the band structure with respect to various perturbations of the Dirac Hamiltonian is proposed [38]. In that study, it is suggested that the pseudogapped Kondo state is stabilized with the line-node Weyl semimetal, which is formed via a lifting of the degenerated Dirac-cone bands along the energy under broken inversion symmetry and conserved time-reversal symmetry. The dense Kondo effect for the Weyl fermion is also expected to arise in a regular Ce-ion lattice with noncentrosymmetry. Our $Ce_3Co_4Sn_{13}$ data exhibit a signature of the $4f$-electron contribution to the Fermi surface. Therefore, we can speculate that the high-resistivity phase of $Ce_3Co_4Sn_{13}$ is the pseudogapped Kondo state originating from the Fermi energy tuned to the band-crossing line node via the dense Kondo effect on the Weyl fermion system. In addition to such a Weyl semimetal mechanism, the emergence of the spatial correlation in the spin dynamics below 15 K is hypothesized to be given by the Ruderman-Kittel-Kasuya-Yoshida interaction, which should be influenced by the Weyl-fermion conduction electrons [39]. We also expect that the noncentrosymmetric structure causes the Dzyaloshinsky-Moriya interaction, as theoretically investigated [39]. The spatial oscillations of the interactions characteristic to the Weyl-fermion band node structure have been discussed. It will be interesting to apply such theoretical arguments to the observed spin dynamics of $Ce_3Co_4Sn_{13}$.

We should also mention the effect of the time-reversal-symmetry breaking on the Dirac fermion system. This effect results in a splitting in the momentum space of the Dirac cone band to form another type of Weyl fermion [39]. The existence of such three-dimensional Dirac or Weyl semimetal has recently been argued for the insulator state accompanied by the magnetic ordering of Ir atoms in pyrochlore iridates $RE_2Ir_2O_7$ [40]. The resistivity enhancement with decreasing temperature has been theoretically derived on the basis of the isotropic Weyl nodes [41]. Based on these theoretical results, we infer that the noncentrosymmetry with a periodic magnetic lattice causes the electrical-resistivity enhancement, accompanied by the particular magnetic correlation owing to the Weyl-fermion bands. $Ce_3Co_4Sn_{13}$ does not undergo any magnetic ordering transition, but the clearly observed dispersing spin excitation suggests that the electronic state is close to the time-reversal symmetry violation. The Ce-based 3-4-13 systems are candidate materials for exhibiting such a Weyl semimetal state in the chiral magnetic lattice.

V. CONCLUSION

The Ce $4f$ electronic state in the chiral-lattice phase of $Ce_3Co_4Sn_{13}$ has been revealed via INS experiments. The entire spectrum can be reproduced by two inequivalent CEF level schemes, which are consistent with the structural superlattice formation [15] and the field-induced antiferromagnetic diffraction peaks [14]. We have observed the dispersing spin dynamics below 1 meV within the Kramers doublet ground states for the two inequivalent Ce-ion sites. The spin dynamics evolves with the steep upturn of the electrical resistivity with decreasing temperature below 15 K [7,13] and causes the specific-heat maximum at 0.7 K [6,8]. Thus, this dynamics is crucial to unveiling of the low-temperature electronic state of $Ce_3Co_4Sn_{13}$. Determining whether the observed spin dynamics and the high-electrical-resistivity phase are peculiar to the chiral crystallographical symmetry that mediates the three-dimensional Weyl fermion is a topic for further investigation.

ACKNOWLEDGMENTS

We thank M. Onodera at Tohoku University for his collaboration. T. Kikuchi and Y. Inamura at J-PARC Center are acknowledged for his assistance in the analysis of AMATERAS data. P. Boutrouille and P. Baroni at Laboratoire Léon Brillouin are acknowledged for their assistance in operating the cryostat and the spectrometer. The crystal-piece alignment was performed using a high-energy x-ray Laue camera with the support of T. Masudas group at ISSP, The University of Tokyo. K. Kaneko is acknowledged for fruitful discussions of the studies on the 3-4-13 series compounds. P. Steffens, S. Raymond, D. T. Adroja, and Z. Fisk are appreciated for their contributions to discussions on the INS data of the 3-4-13 series compounds. This study was supported in part by the Japan Society for the Promotion of Science, KAKENHI Grant No. JP21224008 [Scientific Research (S)], JP23244068 [Scientific Research (A)], JP24654080 [Exploratory Research], JP15H03692 [Scientific Research (B)], and JP17H05209 [Scientific Research on Innovative Areas "3D Active-Site Science"]. The experiment at BL14, the Materials and Life Science Facility, J-PARC, was based on approved Proposals

(No. 2014P0202 and No. 2013B0173). The experiment at 4F2 at the Laboratoire Léon Brillouin was also conducted under an approved proposal (No. 12290). The travel expenses of KI and YO for this experiment were supported by the General User Program for Neutron Scattering Experiments, Institute for Solid State Physics, The University of Tokyo (Proposals No. 15528, No. 15538, No. 16523, and No. 16533), at JRR-3, Japan Atomic Energy Agency, Tokai, Japan.

---

[1] Edited by T. Kasuya and T. Saso, *Theory of Heavy Fermions and Valence Fluctuations* (Springer, Heidelberg, 1985).
[2] Y. Ando, J. Phys. Soc. Jpn. **82**, 102001 (2013).
[3] S. Fujimoto, J. Phys. Soc. Jpn. **76**, 051008 (2007).
[4] E. Bauer, G. Hilscher, H. Michor, Ch. Paul, E. W. Scheidt, A. Gribanov, Yu. Seropegin, H. Noël, M. Sigrist, and P. Rogl, Phys. Rev. Lett. **92**, 027003 (2004).
[5] S. Mühlbauer, B. Binz, F. Jonietz, C. Pfleiderer, A. Rosch, A. Neubauer, R. Georgii, and P. Böni, Science **323**, 915 (2009).
[6] A. L. Cornelius, A. D. Christianson, J. L. Lawrence, V. Fritsch, E. D. Bauer, J. L. Sarrao, J. D. Thompson, and P. G. Pagliuso, Physics B **378–380**, 113 (2006).
[7] E. L. Thomas, H.-O. Lee, A. N. Bankston, S. MaQuilon, P. Klavins, M. Moldovan, D. P. Young, Z. Fisk, and J. Y. Chan, J. Solid State Chem. **179**, 1642 (2006).
[8] A. Ślebarski, B. D. White, M. Fijałkowski, J. Goraus, J. J. Hamlin, and M. B. Maple, Phys. Rev. B **86**, 205113 (2012).
[9] A. Ślebarski and J. Goraus, Phys. Rev. B **88**, 155122 (2013).
[10] A. D. Christianson, J. S. Gardner, H. J. Kang, J.-H. Chung, S. Bobev, J. L. Sarrao, and J. M. Lawrence, J. Magn. Magn. Mater. **310**, 266 (2007).
[11] C. S. Lue, H. F. Liu, S.-L. Hsu, M. W. Chu, H. Y. Liao, and Y. K. Kuo, Phys. Rev. B **85**, 205120 (2012).
[12] H. F. Liu, C. N. Kuo, C. S. Lue, K.-Z. Syu, and Y. K. Kuo, Phys. Rev. B **88**, 115113 (2013).
[13] J. R. Collave, H. A. Borges, S. M. Ramos, E. N. Hering, M. B. Fontes, E. Baggio-Saitovitch, L. Mendonça-Ferreira, E. M. Bittar, and P. G. Pagliuso, J. Appl. Phys. **117**, 17E307 (2015).
[14] A. D. Christianson, E. A. Goremychkin, J. S. Gardner, H. J. Kang, J.-H. Chung, P. Manuel, J. D. Thompson, J. L. Sarrao, and J. M. Lawrence, Physica B **403**, 909 (2008).
[15] Y. Otomo, K. Iwasa, K. Suyama, K. Tomiyasu, H. Sagayama, R. Sagayama, H. Nakao, R. Kumai, and Y. Murakami, Phys. Rev. B. **94**, 075109 (2016).
[16] A. Ślebarski, J. Goraus, and P. Witas, Phys. Rev. B **92**, 155136 (2015), and references therein.
[17] J. L. Mañes, Phys. Rev. B **85**, 155118 (2012).
[18] G. P. Espinosa, Mat. Res. Bull. **15**, 791 (1980).
[19] J. P. Remeika, G. P. Espinosa, A. S. Cooper, H. Barz, J. M. Rowell, D. B. McWhan, J. M. Vandenberg, D. E. Moncton, Z. Fisk, L. D. Woolf, H. C. Hamaker, M. B. Maple, G. Shirane, and W. Thomlinson, Solid State Commun. **34**, 923 (1980).
[20] G. P. Espinosa, A. S. Cooper, and H. Barz, Mat. Res. Bull. **17**, 963 (1982).
[21] K. Nakajima, S. Ohira-Kawamura, T. Kikuchi, M. Nakamura, R. Kajimoto, Y. Inamura, N. Takahashi, K. Aizawa, K. Suzuya, K. Shibata, T. Nakatani, K. Soyama, R. Maruyama, H. Tanaka, W. Kambara, T. Iwahashi, Y. Itoh, T. Osakabe, S. Wakimoto, K. Kakurai, F. Maekawa, M. Harada, K. Oikawa, R. E. Lechner, F. Mezei, and M. Arai, J. Phys. Soc. Jpn. **80**, SB028 (2011).
[22] Y. Inamura, T. Nakatani, J. Suzuki, and T. Otomo, J. Phys. Soc. Jpn. **82**, SA031 (2013).
[23] U. Walter, J. Phys. Chem. Solids **45**, 401 (1984).
[24] W. Marshall and R. D. Lowde, Rep. Prog. Phys. **31**, 705 (1968).
[25] K. Iida, K. Ikeuchi, M. Ishikado, J.-i. Suzuki, R. Kajimoto, M. Nakamura, Y. Inamura, and M. Arai, JPS Conf. Proc. **1**, 014016 (2014).
[26] P. P. Deen, A. M. Strydom, S. Paschen, D. T. Adroja, W. Kockelmann, and S. Rols, Phys. Rev. B **81**, 064427 (2010).
[27] P. Y. Portnichenko, A. S. Cameron, M. A. Surmach, P. P. Deen, S. Paschen, A. Prokofiev, J.-M. Mignot, A. M. Strydom, M. T. F. Telling, A. Podlesnyak, and D. S. Inosov, Phys. Rev. B **91**, 094412 (2015).
[28] U. Köhler, A. P. Pikul, N. Oeschler, T. Westerkamp, A. M. Strydom, and F. Steglich, J. Phys.: Condens. Matter **19**, 386207 (2007).
[29] J. Custers, M. Kriegisch, M. Müller, A. Thamizhavel, A. M. Strydom, and S. Paschen, Physica B **403**, 1312 (2008).
[30] K. Suyama, K. Iwasa, Y. Otomo, K. Tomiyasu, H. Sagayama, R. Sagayama, H. Nakao, R. Kumai, and Y. Murakami (unpublished).
[31] D. T. Adroja, A. M. Strydom, A. P. Murani, W. A. Kockelmann, and A. Fraile, Physica B **403**, 898 (2008).
[32] K. Iwasa, K. Suyama, Y. Otomo, K. Tomiyasu, S. Raymond, P. Steffens, and J.-M. Mignot (unpublished).
[33] B.-J. Yang and N. Nagaosa, Nat. Commun. **5**, 4898 (2014).
[34] Z. K. Liu, B. Zhou, Y. Zhang, Z. J. Wang, H. M. Weng, D. Prabhakaran, S.-K. Mo, Z. X. Shen, Z. Fang, X. Dai, Z. Hussain, and Y. L. Chen, Science **343**, 864 (2014).
[35] H. Li, H. He, H.-Z. Lu, H. Zhang, H. Liu, R. Ma, Z. Fan, S.-Q. Shen, and J. Wang, Nat. Commun. **7**, 10301 (2016).
[36] S.-M. Huang, S.-Y. Xu, I. Belopolski, C.-C. Lee, G. Chang, B. K. Wang, N. Alidoust, G. Bian, M. Neupane, C. Zhan, S. Jia, A. Bansil, H. Lin, and M. Z. Hasan, Nat. Commun. **6**, 7373 (2015).
[37] X. Huang, L. Zhao, Y. Long, P. Wang, D. Chen, Z. Yang, H. Liang, M. Xue, H. Weng, Z. Fang, X. Dai, and G. Chen, Phys. Rev. X **5**, 031023 (2015).
[38] A. K. Mitchell and L. Fritz, Phys. Rev. B **92**, 121109(R) (2015).
[39] H.-R. Chang, J. Zhou, S.-X. Wang, W.-Y. Shan, and D. Xiao, Phys. Rev. B **92**, 241103(R) (2015).
[40] X. Wan, A. M. Turner, A. Vishwanath, and S. Y. Savrasov, Phys. Rev. B **83**, 205101 (2011).
[41] P. Hosur, S. A. Parameswaran, and A. Vishwanath, Phys. Rev. Lett. **108**, 046602 (2012).